The Importance of Decarbonylation Mechanisms in the Atomic Layer Deposition of High-Quality Ru Films by Zero-Oxidation State $Ru(DMBD)(CO)_3$

Joel R. Schneider,[1,†] Camila de Paula,[1,†] Jacqueline Lewis,[1] Jacob Woodruff,[2] James A. Raiford,[1] Stacey F. Bent[1,*]

† Authors contributed equally to this work

[1] Department of Chemical Engineering, Stanford University, Stanford, California 94305, USA

[2] EMD Electronics, Haverhill, Massachusetts 01832, USA

*Email: sbent@stanford.edu

I. Abstract

Achieving facile nucleation of noble metal films through atomic layer deposition (ALD) is extremely challenging. To this end, η^4-2,3-dimethylbutadiene ruthenium tricarbonyl ($Ru(DMBD)(CO)_3$), a zero-valent complex, has recently been reported to achieve good nucleation by ALD at relatively low temperatures and mild reaction conditions. We study the growth mechanism of this precursor by *in situ* quartz-crystal microbalance and quadrupole mass spectrometry during Ru ALD, complemented by *ex situ* film characterization and kinetic modeling. These studies reveal that $Ru(DMBD)(CO)_3$ produces high-quality Ru films with excellent nucleation properties. This results in smooth, coalesced films even at low film thicknesses, all important traits for device applications. However, Ru deposition follows a kinetically limited decarbonylation reaction scheme, akin to typical CVD processes, with a

strong dependence on both temperature and reaction timescale. The non-self-limiting nature of the kinetically driven mechanism presents both challenges for ALD implementation and opportunities for process tuning. By surveying reports of similar precursors, we suggest that the findings can be generalized to the broader class of zero-oxidation state carbonyl-based precursors used in thermal ALD, with insight into the design of effective saturation studies.

II. Introduction

Because thin films play a key role in the development of nanomaterials, with applications in microelectronics,[1] photovoltaics,[2] energy storage,[3,4] and beyond,[5,6] a great deal of attention has been devoted to development of thin film deposition techniques. There is a wide range of strategies for depositing thin films, including sol-gel, sputtering, and evaporation, but atomic layer deposition (ALD) and chemical vapor deposition (CVD) have particular advantages as they excel at depositing material with high quality and uniformity on complex surface structures.[1,7] Substantial effort in the literature has been devoted to understanding growth mechanisms involved in ALD and CVD, often with the goal of depositing a variety of different materials with increasing levels of conformality and uniformity.[7–10]

As vapor-phase deposition techniques, CVD and ALD rely heavily on the chemical interaction between precursors and substrates,[1] meaning surface chemical reactions are of particular importance. Surface reaction pathways have a significant impact on observed growth phenomena,[7,10,19,11–18] and the coordination sphere of a precursor has been found to have a direct effect on various film properties, including crystallinity,[20–22] dielectric constant,[21] and impurity concentration,[23,24] among others.[22,25] Moreover, tuning precursor chemistry by altering the coordination sphere around the metal center has been shown to be a highly effective tool to

enhance film nucleation, resulting in higher growth rates (GR) for CVD or growth per cycle (GPC) for ALD.[26]

Atomic layer deposition relies on self-limiting reactions between the precursor and the surface.[1,7,27] A precursor must achieve a fine balance between reactivity and inertness to be considered suitable for ALD.[25] Namely, a precursor must be sufficiently reactive to bind to the surface, but once it is bound it must be sufficiently inert to resist further reactions with other precursor molecules. If the latter criterion is not met, the deposition process may be categorized as CVD or pulsed CVD.[1,7] This balance of reactivity and inertness can be achieved by partial elimination of precursor ligands, where the remaining ligands on the surface-bound precursor resist further reaction with additional precursor molecules. However, if these retained ligands are too difficult to eliminate, the process can suffer from long nucleation delays, and this effect can be exacerbated by other factors such as sterically bulky precursors, or the oxidation state of the metal center as described below. Unfortunately, despite the broad utility of metallic thin films such as Pt and Ru,[4,28–30] these challenges are common with noble metal ALD.[31]

Because facile nucleation of Ru ALD is highly desirable for applications such as microelectronics, we focus on Ru ALD as a model system in this work.[32,33] A recent report by Austin et al.[34] studied the average nucleation delay for different Ru precursors used in thermal ALD as a function of oxidation state of the metal center. A correlation was observed between the length of nucleation delay and the oxidation state of the precursor, where Ru precursors of lower oxidation state had significantly shorter nucleation delays. More generally, zero-oxidation state precursors have been reported to chemisorb to the surface through a thermally induced, surface-mediated dissociation or dissociative substitution reaction, facilitating rapid nucleation.[35–39] Although this pathway can reduce the self-limiting nature of their reaction with the surface and

make them more challenging to apply to ALD, such precursors have been widely used in the CVD literature.[40–42] While there are many factors that affect nucleation and growth, the reported correlation between oxidation state and nucleation delay raises questions about the reaction mechanisms taking place. These mechanisms, if understood, could provide powerful insights into noble metal precursor design and process development for this notoriously difficult class of ALD and CVD processes. As such, this work focuses on probing the growth mechanism of a zero-oxidation state Ru precursor—described below—that has been used to deposit high-quality Ru films.[34,43–45] We then compare these results to reports on the growth mechanism of other zero-oxidation state precursors to make general observations to inform how they can be applied to ALD and CVD. In particular, we seek to gain insight into three mechanistic questions: (i) since zero-oxidation state precursors may not react with the surface in a self-limiting fashion, what mechanisms could render such precursors suitable for ALD? (ii) since zero-oxidation state precursors usually do not undergo ligand exchange reactions[36,40,46,47] nor change oxidation state, what is the role of the counter-reactant and is it necessary to achieve metallic films? and (iii) what is the general expected relationship between GPC and temperature for a zero-oxidation state precursor?

Recently, several studies have reported the ALD of high-quality Ru films from η^4-2,3-dimethylbutadiene ruthenium tricarbonyl [Ru(DMBD)$(CO)_3$(0)], using either O_2[34,45,48] or various non-oxidative counter-reactants such as H_2O or hydrazine.[43,44,49] The studies indicate that this precursor is an exceptional candidate for Ru vapor deposition, as it is volatile and thermally stable, does not suffer from a nucleation delay on SiO_2, and yields pure and smooth Ru films at relatively low temperatures. Yet, a closer look at the reported GPC as a function of temperature and counter-reactant in the earlier reports reveals significant discrepancies. Gao et

al.[44] reported a constant GPC of 1 Å/cycle at 160-220 °C, whereas the GPC at temperatures above and below this range rapidly declined and increased, respectively, with increasing temperature. The counter-reactant used in that study was H_2O. Using an O_2 counter-reactant, Austin et al.[34] described a similar GPC temperature dependence, but at a different temperature range. The authors reported a constant GPC of 0.8 Å/cycle at 260-280 °C, with a decrease or increase in GPC with increasing temperature at temperatures above or below the 260-280 °C range, respectively. Cwik et al.[43] reported a constant GPC of 0.4 Å/cycle at 200-210 °C and a steadily increasing GPC with increasing temperature both above and below the 200-210 °C range. The counter-reactant in that study was 1,1-dimethylhydrazine. Interestingly, Winter and coworkers observed growth of Ru islands without using a counter-reactant at all.[50]

Across those previous studies, the reported temperatures at which constant GPCs were achieved differ by 60-80 °C, and the reported GPC value differ by 0.2-0.35 Å/cycle. Although some discrepancy in GPC can be expected when using different counter-reactants (water, oxygen, hydrazine), the discrepancies in the trends of the GPC as a function of temperature and the growth of Ru islands without any counter reactant merits further investigation. Furthermore, since other studies have suggested growth using carbonyl-based precursors (such as $Mo(CO)_6$, $Fe(CO)_5$, $W(CO)_6$, $Cr(CO)_6$, $Ru_3(CO)_{12}$) is governed primarily by thermal CO dissociation (i.e., decarbonylation) at elevated temperatures,[36,39,40,51,52] one would expect that beyond the self-limiting regime (if such a regime exists), the GPC would increase sharply with increasing temperature,[36,46,47] the opposite of the reported trend in some of these works. In fact, on acidic oxides such as SiO_2, $Ru_3(CO)_{12}$ has been shown to decarbonylate completely at 200 °C.[53,54] A growth rate that decreases with increasing temperature has been previously reported for Fe CVD from $Fe(CO)_5$,[55] but this behavior has been ascribed to extensive dissociation and

decomposition of CO into inert graphitic carbon on the active Fe surface. Fe is generally regarded to be more reactive towards CO decomposition than Ru,[56] so this mechanism may not be present in the Ru system. In addition, CVD studies of other Ru carbonyl precursors, such as $Ru(CO)_3C_6H_8$, report a trend of increasing GR with temperature, up to temperatures as high as 290 °C.[57] The report by Winter and coworkers on the CVD-like growth of Ru from $Ru(DMBD)(CO)_3$ without the use of a counter-reactant further supports the aforementioned suggestion that elevating temperatures should promote thermal dissociation of the precursor.[50]

Given the open questions about the growth mechanism of the $Ru(DMBD)(CO)_3$ (0) precursor, combined with its excellent deposition characteristics and the aforementioned mechanistic questions, we carry out mechanistic investigations of this precursor in the current study. To elucidate the deposition chemistry of metal carbonyl derivative precursors, we implement *in situ* quartz-crystal microbalance (QCM) and quadrupole mass spectrometry (QMS) to monitor the deposition of $Ru(DMBD)(CO)_3$ (0) as a function of temperature, both with and without water as a counter-reactant. We also use *ex situ* characterization of the deposited films to examine the resulting film properties and gain further insight into the growth mechanisms. Observed trends regarding temperature and counter-reactant are then explained with a proposed growth mechanism and theoretical kinetic modeling, with principles that shed insight into designing the broader class of zero-oxidation state precursors and deposition processes.

III. Experimental Methods

A. Film Deposition, Characterization, and Monitoring

The precursors used in this study were $Ru(DMBD)(CO)_3$ (EMD Electronics, used as received without further purification) and deionized (DI) water. The Ru precursor was contained in a stainless-steel canister that was filled in a nitrogen glove box and sealed with a manual valve. The canister was kept under vacuum once attached to the ALD chamber and maintained at 35-45 °C. The DI water canister was held at room temperature. The purge time between pulses was varied to probe different reaction timescales, and experiments were performed either with the $Ru(DMBD)(CO)_3$ precursor only, or with $Ru(DMBD)(CO)_3$ and H_2O counter-reactant. In addition, three types of pulsing methods were compared: single pulse, micropulse, and multiple pulse (illustrated in Figure 1). These pulsing methods were used for all quartz crystal microbalance experiments; depositions for quadrupole mass spectrometry and *ex* situ analysis will be described below. For depositions with $Ru(DMBD)(CO)_3$ only, experiments with 10 s purge times (referred to as "micropulse" delivery) and depositions with 42 s purge times (dubbed "multiple pulses") both used Ru precursor pulse times of 2 s. For depositions that only used a single pulse of Ru precursor, pulse times were varied between 0.5 s and 4 s. Because precursor partial pressure varied with pulse time, but remained approximately constant across each pulse, precursor delivery was quantified with exposure, approximated by multiplying the maximum partial pressure of precursor delivered to the substrate by the precursor pulse time. For depositions with H_2O, one cycle consisted of a single 2 s Ru pulse followed by a single 2 s H_2O pulse. In order to limit parasitic growth arising from incomplete reactor purging, sufficient time was allowed after the $Ru(DMBD)(CO)_3$ exposure before the start of the H_2O pulse for the purge gas to clear the reactor of vapor-phase precursor. As a result, 10 s purge times were used after Ru

exposure, and a 30 s purge time was used following each H_2O pulse (also shown in Figure 1). The Ru purge time was chosen such that the introduction of H_2O corresponded to the same timescale as the micropulse experiments, allowing conclusions regarding the state of surface ligands after 12 s from the micropulse experiments to also apply to the H_2O experiments when H_2O is introduced. The H_2O purge time was chosen such that the total amount of time between consecutive Ru exposures was the same as in the multiple pulse scheme, permitting more direct comparison between the process with and without water.

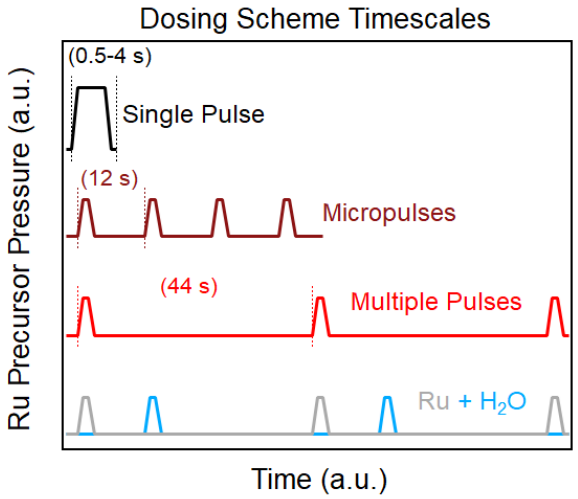

Figure 1. Schematic illustrating the Ru precursor dosing schemes and reaction timescales associated with each. Also shown is the dosing scheme for depositions containing both the Ru precursor and H_2O, with the alternating $Ru(DMBD)(CO)_3$ and H_2O pulses shown in grey and blue, respectively. In the Ru + H_2O scheme, the purge times are such that the Ru pulses align with the multiple-pulse experiments and the time H_2O pulses align with the micropulse experiments.

Depositions of thin films were performed in two different custom-built, cross-flow ALD reactors with 1.75-inch diameter tubular bodies. In cases where deposition was performed on coupons for *ex situ* analysis, the substrates were placed on a flat steel sample holder resting on the bottom of the tubular body. Precursors were introduced near the front door of the reactor and

chamber temperature was modulated in a hot-wall fashion. Reactor pressure was monitored using a convectron gauge.

In the first reactor, the working pressure was maintained in the range of 500-800 mtorr with 10-15 SCCM flow rate of nitrogen purge gas. The range of pressures and exposures during the different experiments are detailed in the Results and Discussion section. The sample holder and a quartz crystal microbalance (QCM) sensor head were in close proximity at the rear of this reactor. The QCM was used for *in situ* monitoring of mass uptake during the deposition process. The QCM was a Colnatec Eon-Tempe system fitted with a RC quartz crystal substrate designed for a 20 °C – 250 °C temperature range. Prior to deposition, the crystal was coated with a thick layer of Ru, which served as the growth substrates for all QCM experiments. The temperature of the crystal substrate was monitored through an internal thermocouple. The rear side of the crystal was sealed off to reduce deposition on the back. Deposition was monitored using a Colnatec and Eon control and monitoring package with universal oscillator. Temperature and mass gain of the crystal substrate were recorded concurrently at a sampling interval of 0.5 seconds. All depositions on substrates for *ex situ* analysis were also done in this reactor, using n-doped (100) Si coupons with native oxide (WRS Materials). The coupons were first cleaned for 15 minutes in a Novascan PSD Series Digital UV Ozone System. During deposition, the temperature of the substrate and QCM sensor head were varied between 80 °C and 180 °C in a hot-wall fashion, using external heating tapes around the reactor body. To probe the mechanistic behavior across a range of temperatures, deposition temperatures in this reactor were held at 80 °C, 100 °C, 125 °C, and 180 °C. To minimize inconsistencies arising from variability in reactor wall conditions or other effects, a full series of deposition experiments were performed consecutively before running other processes on the reactor.

In situ quadrupole mass spectrometry (QMS) was performed in the second reactor. Ultra-high purity 5.0 grade (99.999%, Praxair) argon was used as the carrier gas. Ar was selected for these QMS experiments to avoid m/z=28 mass signal from N_2 purge gas. During deposition, the reactor temperature was monitored and modulated in a hot-wall fashion, using internal and external K-type thermocouples and external heating tapes. The reactor temperature was varied between room temperature (~25 °C) and 125 °C. The QMS (SRS RGA200) was attached downstream of the reactor and was separated from the reactor by a needle valve, and the QMS was monitored and controlled using the RGA software package from Stanford Research Systems. The QMS was pumped on by a turbo pump separate from the main chamber pump, and measurements were taken by opening the needle valve to the QMS. For all QMS depositions, the entire reactor interior walls were used as the reaction surface to study deposition. This approach was selected both because heating of the entire reactor meant surface reactions would take place on the walls and because using a larger reaction surface area maximizes signal for QMS. Depositions were only performed after the reactor interior had been thoroughly coated in metallic Ru, ensuring surface conditions consistent with those of the QCM depositions. For deposition, both the Ru precursor and water were dosed for 1 second. The dosed partial pressures of both reactants were approximately 300-800 mtorr, resulting in total exposures in same range as the exposures obtained in QCM experiments. $Ru(DMBD)(CO)_3$-only depositions contained a 42 s purge time following each pulse, and depositions with $Ru(DMBD)(CO)_3$ and water used purge times of 5 s, 10 s, and 30 s after the Ru precursor with H_2O purge times of 85 s, 80 s, and 60 s, respectively, such that the total time between the start of each $Ru(DMBD)(CO)_3$ pulse remained constant at 92 s. These process parameters were used rather than those shown in Figure 1 due to the increased times required for the second reactor and QMS to be fully purged.

The QMS was run in one of two modes during depositions: analog survey mode or P vs. T channel mode. Survey mode was used to scan across the full m/z range of 0 to 105, and was implemented at room temperature to measure the $Ru(DMBD)(CO)_3$ cracking pattern and at elevated temperatures prior to each deposition to verify consistency of the background and absence of any unexpected gaseous impurities. Survey mode data for the cracking pattern was taken at a single time point when the QMS intensity was greatest. Channel mode data was collected by measuring QMS intensity only at a fixed set of m/z values as a function of time. The measured m/z values were 18 (H_2O), 28 (CO), 44 (CO_2), 67 (DMBD fragment), 82 (DMBD fragment), and 102 (Ru), and one measurement was taken per second. For $Ru(DMBD)(CO)_3$-only depositions, partial pressures of species were determined as follows. Because CO, CO_2, and DMBD all reached their maximum intensities at nearly the same time, the time of peak intensity was determined by finding the maximum of the CO intensity, which was the species with the highest signal. The partial pressures of other species were then extracted from their corresponding intensities at the same point in time as the CO maximum. To test the validity of this approach, other time points near the time of peak intensities were also analyzed, and similar trends to what is reported herein were observed. These characterizations were repeated 20 times for each temperature, with resulting values averaged across the data set to increase the quantitative accuracy of the measurement. For depositions with both $Ru(DMBD)(CO)_3$ and H_2O, channel mode was used to qualitatively detect CO_2 production upon the introduction of H_2O, by obtaining time-resolved profiles of CO_2 intensity (m/z = 44 channel) over time. For each temperature and timescale combination, the process was characterized using 2-5 profiles. For each condition, the individual CO_2 profiles were shifted in time to align the starts of each

$Ru(DMBD)(CO)_3$ pulse, and the profiles were averaged by averaging the CO_2 intensity at each time point within the profiles.

Deposited films were characterized by X-ray photoelectron spectroscopy (XPS), X-ray diffraction (XRD), X-ray reflectivity (XRR), and atomic force microscope (AFM). All samples for *ex situ* characterization were deposited using 20 s purge times following $Ru(DMBD)(CO)_3$ pulses (and H_2O pulses, if used), resulting in total reaction timescales comparable to those in shown in Figure 1 for depositions with H_2O and timescales in between micropulse and multiple pulse for precursor-only depositions. The exception is the single experiment at 80 °C where 60 s purges were used to allow for more complete purging and ligand removal at the low temperature. XPS was carried out using a PHI 5000 VersaProbe III with a monochromatic Al K-alpha X-ray source. Measurements were taken using a 200 μm X-ray spot size. Depth profiles were obtained by *in situ* Ar^+ ion beam sputtering at 1kV energy with a current of 0.8 μA over a 2 μm x 2 μm spot in 30 second increments. Between each increment, a high-resolution XPS spectrum was acquired. XPS data analysis was performed using the MultiPak software package.

XRD and XRR were carried out using a PANalytical X'Pert PRO X-ray diffractometer with Cu K-alpha radiation. XRR measurements were collected over 2θ range of 0-8°, whereas XRD measurements were collected over 2θ range of 25-60° with ω at 1°. XRR data was modeled using Nika software package in Igor 7.[58] The electron density was calculated by normalizing the scattering length density (SLD) to that of silicon. The model consisted of an infinite backing substrate of Si with SLD 20.1×10^{-6} Å^{-2} and roughness of 1 Å, covered by an interfacial layer of SiO_2 with a thickness of 15 Å, an SLD of 18.9×10^{-6} Å^{-2}, and a roughness of 1 Å. A fixed background intensity of 1×10^{-7} consistent with the data was used in modeling reflectivity. Ru

layer thickness, SLD, and roughness were all fitted using a genetic algorithm and were the only parameters that were allowed to vary.

Surface morphology and roughness were investigated using a Park NX10 AFM operated in noncontact mode with a MikroMasch NSC35 probe and scanned areas of 1 μm x 1 μm and 0.5 μm x 0.5 μm.

B. Data Analysis & Kinetic Modeling

From QCM measurements, the net mass gain for each $Ru(DMBD)(CO)_3$ exposure was calculated by subtracting the mass before and after each pulse. The resulting mass gains as a function of exposure were then fitted using linear least squares regressions. For the micropulse and multiple-pulse regimes (illustrated in Figure 1), the linear fitting was performed over the entire sequence of pulses, which for deposition temperatures of 80 °C and 100 °C corresponded to cumulative exposures ranging from 0 mtorr-s to roughly 6000-8000 mtorr-s, and for deposition temperatures of 125 °C and 180 °C ranging from 0 mtorr-s to approximately 2000-4000 mtorr-s. Lower exposures were needed at higher temperatures due to increased growth rates at those conditions. At all temperatures, the linear regressions for the micropulse and multiple pulse experiments were performed with the vertical intercept of the fit fixed at zero. In the single-pulse regime, the linear regressions were only performed within the linear regimes of the data, corresponding to non-self-limiting growth. For the deposition temperatures 100 °C, 125 °C, and 180 °C, the regimes fitted by linear regression for these single pulse experiments consisted of measurements taken above 500, 250, and 200 mtorr-s of $Ru(DMBD)(CO)_3$ exposure,

respectively. The slopes resulting from these fits of the single-pulse regime data are termed non-limiting mass gain per exposure throughout this work.

For all linear regressions, the slope was extracted to determine the average mass gain per exposure, and 95% confidence intervals for the slope were calculated. In the micropulse and multiple-pulse regimes, because each data point represents a single measurement, the confidence intervals were constructed from the distributions arising from the linear least squares fitting procedure. For the single-pulse data, each point used in the regression is the average of multiple measurements, so the individual variances of each data point were considered in constructing a confidence interval by using a parametric bootstrap algorithm. The algorithm assumed normally distributed random error in both exposure and mass gain, with standard deviation equal to that of the sample standard deviation calculated from the individual data points. The algorithm was carried out with 10,000 iterations, a value determined to result in sufficient convergence of the simulated data as repeated simulations did not result in variations in results of more than 1-2% and increased iterations did not significantly alter the output of the algorithm. The confidence interval was constructed symmetrically from the resulting simulated distribution of fitted slopes, excluding an equally weighted 2.5% in each the upper and lower tails of the distribution. A more detailed description of the implementation of this algorithm is given in the Supplemental Information.

For statistical analysis of CO_2 profiles measured by QMS, a hypothesis test was performed to determine whether there was a statistically significant difference between the measured CO_2 intensities between two profiles. The null hypothesis used in each comparison was that the true mean intensity of the short timescale profile was less than or equal to that of the baseline, and the alternative hypothesis was that the population mean of the short timescale

profile was greater than that of the baseline. The confidence level used was $\alpha = 0.05$. The hypothesis tests were performed on the difference of the population means using the multiple profiles that were averaged to calculate each CO_2 profile and by assuming the error at each time point was normally distributed. A Student's t distribution was used as the test statistic, the standard error was calculated according to the formula $SE = \sqrt{\frac{s_1^2}{n_1} + \frac{s_2^2}{n_2}}$, and the degrees of freedom were calculated according to $DF = \left(\frac{s_1^2}{n_1} + \frac{s_2^2}{n_2}\right)^2 / \left(\frac{\left(\frac{s_1^2}{n_1}\right)^2}{n_1 - 1} + \frac{\left(\frac{s_2^2}{n_2}\right)^2}{n_2 - 1}\right)$ rounded to the nearest whole integer, where s_i are the sample standard deviations and n_i are the sample sizes. This hypothesis test was performed individually at each point in time that the profiles were collected to determine if the two profiles' intensities exhibit statistically significant differences at each point in time for each temperature and timescale condition.

Kinetic modeling was performed by fitting a multidimensional model to the calculated non-limiting mass gain per exposure resulting from the regression methods described above. In the fitting, the dependent variable was non-limiting mass gain per exposure, and the two independent variables were temperature and reaction time. Due to the non-linear nature of the kinetic model, a non-linear least squares regression was used to fit the model to the data, minimizing the sum of the squares of the residuals between the model and the data. The quantitative structure of the model, the degrees of freedom of the fitting, and the physical definitions of the fitted parameters are described in the Results & Discussion. The 95% confidence interval constructed from this fitting procedure was calculating using another parametric bootstrap algorithm using the errors calculated above for non-limiting mass gain per exposure at each temperature and timescale. Because the propagated error distributions were

generally symmetrical, for simplicity in this bootstrap they were all approximated as normal with the previously calculated 95% confidence intervals corresponding to 1.96 standard deviations. The parametric bootstrap was implemented in a manner similar to the previous bootstrap but with 1,000 iterations, and a symmetric 95% confidence interval for the bond energy was constructed from the distribution of fitted parameters to the simulated data.

IV. Results & Discussion

A. *In Situ* Reaction Monitoring by QCM

Deposition of the $Ru(DMBD)(CO)_3$ precursor on an SiO_2 or SiO_2-covered Si substrate over a range of temperatures, with and without H_2O as a counter-reactant, was monitored with *in situ* tools to learn about the chemical reactions taking place at the surface. QCM measurements were used to examine saturation behavior of the precursor. Because self-limiting growth in ALD can be dependent on both precursor exposure and purge time, both parameters were varied during the QCM experiments. Throughout this work, precursor pulse and purge sequences were modified to probe three separate timescales, as described in Figure 1. Precursor delivery regimes for which the entire exposure is delivered within one pulse with no intermittent purge times is referred to as "single pulse," with the surface reactions monitored only during the duration of a single pulse time. The total reaction timescale probed by QCM during "single pulse" is 3 s. A "micropulse" delivery refers to the purge regime in which the total precursor exposure is divided into multiple equal smaller exposures separated by short intermediate purge times, stretching out the reaction timescale to 12 s before the subsequent pulse arrives. The final purge timescale explored is referred to as "multiple pulses" and describes a similar delivery schema of multiple equal smaller exposures but each separated by longer purge times, with a total reaction time of

44 s for each pulse. Mass uptake measurements taken at each of these purge conditions across a temperature range of 100 – 180 °C for a range of exposures of the $Ru(DMBD)(CO)_3$ precursor alone (no counter-reactant) are shown in Figure 2. For the same exposures in Figure 2, the three pulse schemes access three different timescales. As an example to illustrate the timescale differences, data points at 1500-1600 mtorr-s of precursor exposure at 100 °C (Figure 2a) can be compared: the black single pulse point was measured with one pulse for a total experiment time of roughly 3 s, the dark red micropulse point consisted of five separate micropulses—each with an individual reaction time of 12 s—for a total experiment time of 60 s, and the light red multiple-pulse point consisted of two separate pulses of 44 s timescales for a total experiment time of 88 s. Measurements were also taken at 80 °C (shown in Figure S1), but due to the low mass uptakes observed, the gains are the same magnitude as the resolution of the instrument. As such, measurements at 80 °C were limited to only the micropulsing delivery regime.

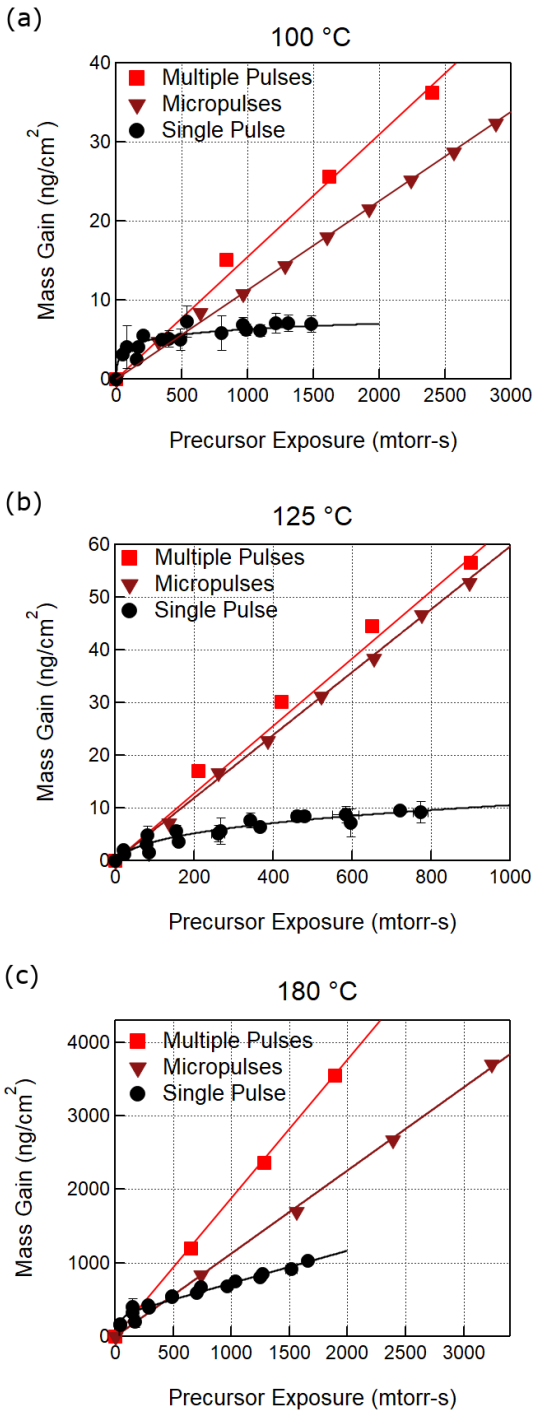

Figure 2. Mass gain measured by QCM of $Ru(DMBD)(CO)_3$-only exposures at (a) 100 °C, (b) 125 °C, and (c) 180 °C as a function of precursor exposure, comparing the three different reaction timescales at each temperature (roughly 3 s, 12 s, and 44 s for single pulse, micropulse, and multiple pulse, respectively). The black curves and the light and dark red lines are guides to the eye.

At 100 °C, as seen in Figure 2a, the single pulse data reveal that growth resulting from $Ru(DMBD)(CO)_3$ is self-limiting, a hallmark feature of ALD. The growth plateaus at mass uptake values around 6 ng/cm^2, indicating that the surface reaction terminates after around 300 mtorr-s of precursor exposure and that the surface is passivated against further reaction beyond this exposure. The density of Ru is 12.45 g/cm^3, so a monolayer thickness of 2.1 Å would correspond to roughly 250 ng/cm^2 of mass uptake.[59,60] Thus, at 6 ng/cm^2, the amount of Ru deposited under these saturating conditions is only a small fraction of a monolayer.

Interestingly, at both longer reaction timescales and higher temperatures, this self-limiting behavior is lost. As shown by the dark and light red data in Figure 2a, when the precursor exposure is divided into multiple smaller separate pulses over a longer timescale, growth continues in a linear fashion with exposure. This trend is also apparent at all other temperatures (Figure 2b-c, Figure S1), with higher mass gains per exposure observed at higher temperatures. At elevated temperatures, particularly by 180 °C, non-saturating growth is observed for the single pulse timescale as well. Together, these QCM observations are consistent with a mechanism in which surface passivation is lost with increasing time and temperature. Since surface passivation in vapor processes like ALD and CVD typically comes from persisting ligands[1,7,17] and no co-reactant was used in these experiments, the QCM data suggest that there are spontaneous surface reactions that remove or otherwise degrade the passivating surface ligands over time to reactivate the surface to reaction with Ru precursor, and that this process accelerates at increased temperature. Because all of the ligands on $Ru(DMBD)(CO)_3$ are L-type ligands, meaning their bonds to the Ru metal center are dative covalent bonds, they can be removed without changing the oxidation state of the Ru center; therefore, simple desorption of the ligands is a possibility.

To further probe the growth mechanism of the Ru precursor, depositions were also performed with $Ru(DMBD)(CO)_3$ and H_2O included as a counter-reactant, with one pulse of H_2O following each Ru precursor pulse as depicted in Figure 1. The purge time following the water exposure was such that the total time between subsequent Ru precursor pulses corresponded to that of the multiple pulse timescale. All depositions with H_2O were performed at 100 °C, 125 °C, and 180 °C. The resulting QCM measurements (Figure S2) suggest that the presence of the H_2O counter-reactant does not have a significant effect on film growth for the following reasons. First, at all three temperatures, no significant sustained mass decrease with H_2O exposure—which could indicate ligand removal—is observed. Initial transient behavior is not unexpected,[61] and the data suggest that as the crystal equilibrates and the H_2O is purged from the reactor, the mass returns to the initial value. It is possible that H_2O exposures could play more of a role at shorter timescales after the $Ru(DMBD)(CO)_3$ exposures, but as seen at 100 °C in Figure S2a, the timescales required for QCM crystal equilibration and reactor purging limit the capability of these measurements to probe H_2O participation at shorter timescales. Second, when compared to the Ru-only measurements in Figure 2, mass gains due to $Ru(DMBD)(CO)_3$ exposures were consistent with the precursor-only experiments. Given the Ru precursor exposures used in each, the mass gains in Figure S2a-c correspond roughly to mass gain per exposures of 14.7, 68.5, and 1750 ng/cm^2-torr-s respectively, close to those of the multiple pulse regime in Figure 2a-c (14.9, 63.1, and 1850), represented by the slopes of the light red lines. The similarity of the growth behaviors with and without water further indicates H_2O exposures do not appear to have a significant impact on growth under these conditions.

B. *In Situ* Reaction Monitoring by QMS

To further study the surface reactions related to ligand removal, *in situ* QMS experiments were performed to analyze the gaseous byproducts of the surface reactions. To allow for direct observation of CO ligand desorption, Ar was used as the purge gas instead of N_2 (as was used in QCM experiments) because unlike N_2, Ar (m/z=40) will not obscure the CO mass peaks. The room temperature cracking pattern of $Ru(DMBD)(CO)_3$ and background QMS measurement are shown in Figure S3. The observed peaks are consistent with the work of Gao et al.[44], and our cracking pattern measurement gave rise to the m/z values monitored in QMS channel mode as described in Methods. CO_2 was monitored by QMS for two reasons: firstly it can be produced as a product of the fragmentation process inside the QMS from the Ru precursor itself as seen from the cracking pattern, and secondly it could be produced as the result of CO ligand elimination by H_2O through the water-gas shift (WGS) reaction as proposed by Gao et al.[44] While previous reports in heterogenous catalysis indicate Ru has low activity toward the WGS reaction at these temperatures,[62–66] given the report by Gao et al.[44] and the observation of Ru WGS activity in some homogeneous catalysis studies,[44,67–69] we investigate it here as a possible mechanism. Because m/z = 67 was found to be the most intense peak for DMBD (Figure S3), this channel was used in quantification for the DMBD species. Since the peak at m/z = 102 for Ru is very low intensity, its low signal-to-noise ratio precluded its use for any quantitative analysis in this work. In addition to the peaks corresponding to species from Ru precursor fragments or reaction products, H_2O (m/z = 18) was measured because it was used as a co-reactant.

After collection of the room temperature cracking pattern shown in Figure S3, two *in situ* experiments were performed and monitored by QMS during deposition, one with $Ru(DMBD)(CO)_3$ only and one with both $Ru(DMBD)(CO)_3$ and H_2O. In the former, repeated

$Ru(DMBD)(CO)_3$ exposures performed in the multiple pulse timescale were measured by QMS in channel mode, as described in Methods. The measurements were made at 100 °C and 125 °C, and the resulting raw data is shown in Figure S4. From this data, the average ratio of DMBD to CO in the gaseous byproducts was determined according to the analysis procedure described in Methods and plotted as a function of temperature in Figure 3. At room temperature (ratio calculated from data in Figure S3), no reaction is expected between the precursor and the reactor walls because the precursor is stable at room temperature, and the DMBD/CO ratio of approximately 0.06 corresponds to the peak ratio from the precursor cracking pattern. The trend of increasing DMBD/CO ratio with increasing temperature seen in Figure 3 indicates that in addition to the baseline signal of DMBD and CO from unreacted precursor, preferentially more gaseous DMBD than gaseous CO is produced by reaction of the precursor at the wall surface, and that the relative production of DMBD over CO by the wall reaction increases from 100 °C to 125 °C. Note that in Figures S3-4 the background signals at m/z = 28 and 67 in the absence of the Ru precursor do not vary significantly as a function of temperature, so the trend in Figure 3 is attributed fully to reactions involving the Ru precursor. This result is consistent with density functional theory calculations predicting the dissociation of the DMBD rather than CO ligands in the chemisorption of $Ru(DMBD)(CO)_3$ to the surface,[44] as well as with our QCM measurements that show increased deposition rates at 125 °C compared to 100 °C.

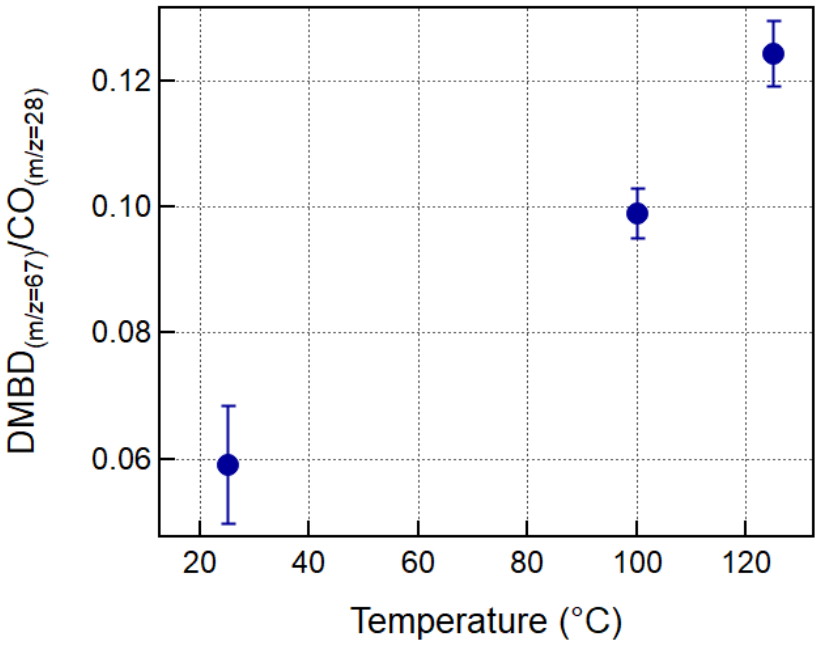

Figure 3. Ratio of DMBD intensity (m/z = 67) to CO intensity (m/z = 28) as measured by QMS as a function of reactor temperature. Error bars represent one standard deviation of all averaged measurements.

In the other QMS experiment, both $Ru(DMBD)(CO)_3$ and H_2O pulses were used to probe the extent to which H_2O participates in surface reactions. Because a previously proposed mechanism for this ALD half-reaction is the WGS reaction to produce CO_2,[44] occurrence of this reaction was probed by monitoring CO_2 partial pressure over time. Depositions were performed at both 100 °C and 125 °C with varying Ru precursor purge times before the introduction of H_2O. The resulting CO_2 profiles were measured by QMS and averaged according to the procedure described in Methods, and the resulting profiles are shown in Figure S5. At both temperatures, the CO_2 profiles are similar regardless of timescale between the Ru precursor and H_2O exposures. Although detection of CO_2 as a gaseous byproduct could indicate participation of H_2O in the WGS reaction with persisting surface CO ligands, CO_2 is also present in the cracking pattern of $Ru(DMBD)(CO)_3$ and thus is expected during the Ru precursor pulse. Hence,

the locations of note in these profiles are the regions of each profile shortly after the time when water was introduced into the reactor, as marked by the colored dashed lines. Because a 30 s purge is nearly enough time for the entire CO_2 signal to rise and decay back to the background even with no introduction of H_2O, the signal in the 30 s profile at times prior to 30 seconds is assigned purely to the CO_2 contributions from $Ru(DMBD)(CO)_3$.

Comparing the 30 s profile baselines to the 5 s and 10 s purge profiles by visual inspection to identify minor increases in CO_2 intensity after the dashed lines in Figures S5a-b is not fruitful because of the low signal-to-noise ratio. Therefore, a more rigorous statistical analysis (detailed in Methods) was used to determine if the differences between the 5 s and 10 s profiles and the 30 s baseline profile are statistically significant. Through this analysis, it is determined that at both 100 °C and 125 °C, neither the 5 s nor 10 s profiles are statistically significantly greater than the baseline 30 s profiles at any point in time, except for two time points in the 5 s CO_2 profile at 125 °C. The 5 s CO_2 profile at 125 °C is greater in intensity than the 30 s baseline profile with statistical significance only at the time points 7 and 8 seconds after the start of the Ru pulse, corresponding to 1 and 2 seconds after the start of the H_2O exposure. Although this finding could indicate the presence of small amounts of CO_2 production resulting from a surface reaction with H_2O, the statistical significance is limited to only 2 of the 35 time points in only 1 of the 6 deposition conditions tested. This analysis indicates either that the production of CO_2 by such a reaction is very limited, that the observation is an artifact of the low signal-to-noise ratio and instrumental limitations, or both. As a result, our QMS measurements do not find clear or robust evidence of H_2O participation in a water-gas shift reaction.

C. Film Characterization

To further investigate the fate of the CO ligands, and to compare the chemical and physical properties of the film to the desired properties of Ru thin films, the deposited films were characterized by XPS, XRD, AFM, and XRR. XPS measurements, one of which is shown in Figure 4, indicate the presence of an oxide on the surface of the ruthenium films with the bulk of the films being high-purity metallic Ru. This surface oxide could be formed either from the ALD process itself or from exposure of the samples to atmosphere upon removal from the reactor, but regardless the oxide is confined to the surface region of the film, and this behavior is consistent with previous reports.[34,43,44] High-purity metallic Ru in the bulk of the films is consistent across a range of temperatures and with and without H_2O as a counter-reactant (Figure S6).

Because the C 1s peak overlaps with the Ru 3d peak and its low sensitivity factor causes small fluctuations in peak area to result in large changes in apparent atomic percentage, deconvoluting these peaks is difficult and prone to error, and so we do not use these measurements to extract carbon concentration. However, the Ru 3d doublet alone produces a good fit without needing to add a C 1s contribution, suggesting the absence of significant carbon content. In addition, since the measured Ru 3d doublet is consistent in binding energy, peak position and separation with previous reports, we expect the carbon content to be comparable to Austin et al. where the concentration was below the detection limit.[34] Furthermore, as shown in Figure 4b and Figure S6a-b, we do not observe significant oxygen content within the bulk of the film for samples deposited both with and without the H_2O counter-reactant. Hence, the XPS data do not indicate incorporation of persisting CO ligands into the film in either deposition mode. This result is consistent with the QCM and QMS measurements which suggest that within the range of conditions under which the films measured in Figure 4 and Figure S6 were deposited,

water is not required to remove passivating CO ligands and has little effect on the chemical state of the resulting film.

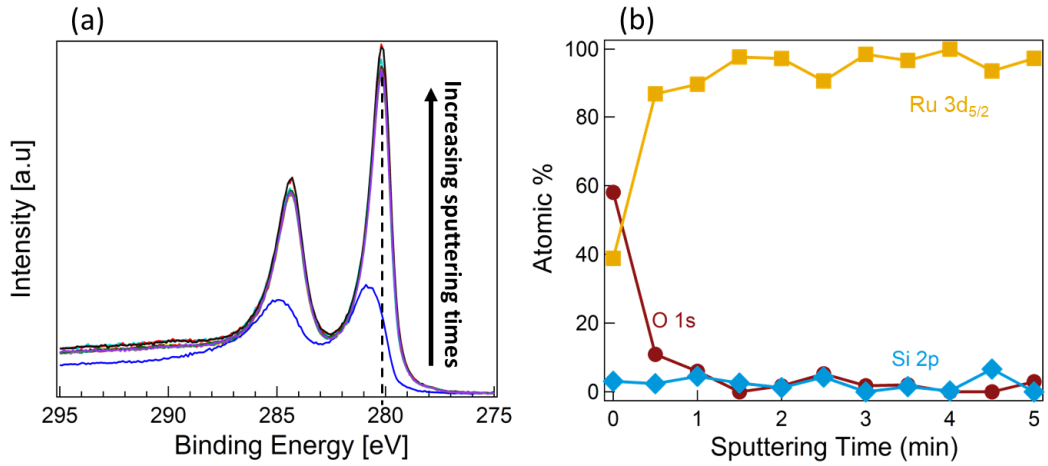

Figure 4. (a) High resolution XP spectra of Ru 3d depth profile after Ru deposition of 100 cycles of $Ru(DMBD)(CO)_3$ (without H_2O) at 180 °C. The arrow indicates the direction of increasing sputtering times. The spectrum in blue, which is shifted to higher binding energies relative to the other spectra, was acquired prior to sputtering (i.e. 0 sputtering time), indicating the presence of surface oxide. The dashed line indicates the center of the Ru $3d_{5/2}$ peak after sputtering. (b) Ru 3d depth profile with Ar ion sputtering in 30 s increments.

In addition to XPS studies, AFM and XRD measurements were performed to investigate the morphology of the deposited films. AFM measurements (Figure S7) show the films deposited with H_2O are very smooth with root mean square roughnesses under 1 nm, even after only 50 cycles of Ru precursor and H_2O (corresponding to a thickness of approximately 50 nm). Many metal ALD processes exhibit poor nucleation behavior resulting in island growth and nanoparticle formation,[11,70] so these measurements indicate excellent nucleation properties of the ALD process and uniform film coalescence at a low number of cycles. XRD measurements shown in Figure S8 reveal that despite their low roughness, the films (grown both with and without H_2O) contain crystalline regions at 180 °C. The crystalline phase also aligns much more

closely to Ru than to RuO_2, in agreement with the XPS results in Figure 4 and Figure S6. A Scherrer analysis of the feature in Figure S8 around $2\theta = 42.5°$ yields an approximate crystallite size of 1.7 nm, consistent with growth of many small nuclei, as expected for a process with little nucleation delay, rather than fewer larger nuclei that may result from a process with a significant nucleation delay.[70] Importantly, the XRD results are indistinguishable for the films deposited with and without H_2O, consistent with the observation by QCM, QMS, and XPS that H_2O does not have a significant impact on the deposition or film properties.

Finally, to support these observations, XRR was performed on films deposited at both 80 °C and 180 °C to assess their thicknesses, densities, and roughness. A deposition temperature of 180 °C was chosen because it was also used for XPS, AFM, and XRD, while 80 °C was selected to explore the possibility that CO ligands might persist for longer timescales at lower temperatures. XRR of a film deposited with both $Ru(DMBD)(CO)_3$ and H_2O at 80 °C is shown in Figure 5a, overlaid with the corresponding fitted model. The model fits all major features of the data, indicating it is of appropriate structure to capture the properties of the film. The model of the 80 °C sample yields a film roughness of 0.6 nm, a thickness of 30.9 Å, and a scattering length density (SLD) of 12.6×10^{-6} Å^{-2}. The small thickness—corresponding to a growth per cycle (GPC) of less than 0.1 Å/cycle—is consistent with the low mass uptake observed by QCM in Figure S1. Converting the SLD values to electron density and then to mass density, the model yields a density of 1.67 g/cm^3, far below that of metallic Ru and only 1.5-2 times as much as many organic polymers.[59,60,71] The low density implies the majority of the film grown at 80 °C is not Ru and instead contains significant organic components. This result would be consistent with ligand incorporation into the film, which could result from a lack of thermal energy to

eliminate ligands from the surface; it will be explored as a possibility in the following subsections.

On the other hand, Figure 5b-c, which illustrate the measurements and models of Ru films deposited at 180 °C with and without water, exhibit very different behavior from Figure 5a. In both cases the model fits the features of the data well, but the model does decay slightly more slowly than the data at higher values of Q. For the films without and with H_2O, the model fits yield roughnesses of 0.4 nm and 0.7 nm, thicknesses of 258 Å and 248 Å, and SLDs of $60.6x10^{-6}$ $Å^{-2}$ and $63.4x10^{-6}$ $Å^{-2}$, respectively. The roughness of the films closely matches the value of 0.5 nm determined by AFM in Figure S7, further lending credence to the results of the XRR model. The modeled thicknesses correspond to average GPCs of 2.5-2.6 Å/cycle, although given the non-limiting growth seen in Figure 2 under these conditions, this GPC is expected to be highly dependent on precursor exposure and could vary significantly. Converting the SLD values to electron density and then to mass density, the model yields densities of 8.05 g/cm^3 and 8.42 g/cm^3 for the respective films. These densities are less than that of Ru (12.45 g/cm^3)[59,60] but can be explained by further examining the deviation between the model and the data at larger incidence angles.

In comparing the XRR model and the data, the two primary features are the fringes and the overall decay. The fringes in the XRR signal correspond to the thickness and roughness of the Ru layer, whereas the overall decay of XRR intensity with increasing Q is generally correlated to the density of the film, although the relationship is complex.[72,73] The excellent agreement between the model and data in the fringes of the spectrum indicates the Ru thickness and roughness predicted by the model are likely more accurate than the density. Whereas the overall decay of the model matches the XRR signal decay relatively well at lower values of Q,

the fit is not quite as good a match at higher values of Q. Because shallower angles of incidence (corresponding to lower values of Q according to the relationship $Q = 4\pi \sin(\theta) / \lambda$) are much more sensitive to the surface region of the film, the better fit at angles at or below the critical angle and the worse fit at larger angles implies the density predicted by the model is closer to that of the surface density and less closely aligned with that of the bulk. As documented elsewhere, this discrepancy corresponds to a density inhomogeneity in the film,[13] with the density extracted from the model being lower than the true bulk density. This interpretation agrees with the presence of the surface oxide detected by XPS, explaining why the modeled densities are skewed closer to RuO_2 (6.97 g/cm^3) than to Ru (12.45 g/cm^3).[59,60] Indeed, instead of using the direct outcome of the model to determine the mass density, estimating a mass density by dividing the mass uptake from QCM by the more well-fitted thickness from XRR yields values in the range of 9.7-13.6 g/cm^3, consistent with metallic Ru. Therefore, XRR measurements of these two films indicate deposition of smooth, pure metallic Ru with a surface layer of ruthenium oxide, consistent with the previous XPS, AFM, and XRD characterizations.

Taken together, the film characterization indicates that at deposition temperatures of 100 °C and above, regardless of whether H_2O is included in the process, metallic Ru films can be deposited with low impurity content. This result is consistent with our QCM and QMS findings that water is not needed to remove CO ligands from the surface to prevent their incorporation into the film. Furthermore, the low film roughnesses observed by XRR and AFM point to a facile precursor chemisorption reaction with little nucleation delay, consistent with the small crystallite size seen by XRD. This facile reaction predicted to occur through the labile and preferential release of DMBD[44] is also observed during chemisorption by QMS. Finally, at a lower

temperature of 80 °C, XRR measurements find incorporation of CO species into the film, pointing to the increased persistence of CO ligands predicted at lower temperatures by QCM.

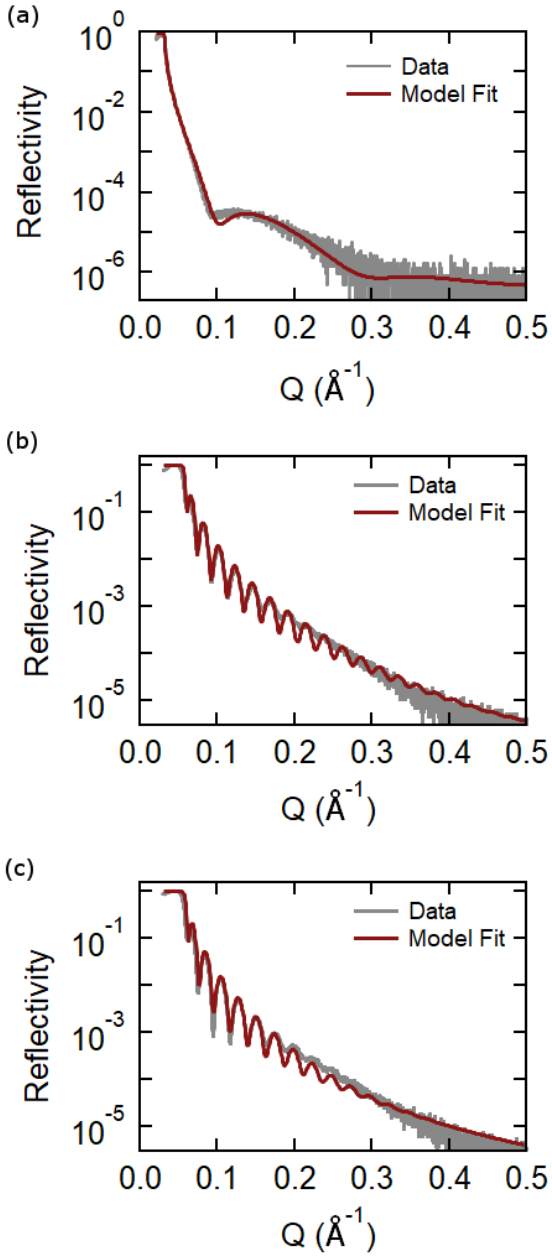

Figure 5. XRR measurement and fitted model of Ru films deposited with (a) 500 cycles of Ru(DMBD)$(CO)_3$ and H_2O at 80 °C, (b) 100 pulses of Ru(DMBD)$(CO)_3$ only at 180 °C, and (c) 100 cycles of Ru(DMBD)$(CO)_3$, and H_2O at 180 °C. The Ru precursor was introduced according to the micropulse dosing scheme in all three depositions.

D. Growth Mechanism

The experimental observations are consistent with a growth mechanism in which the Ru precursor dissociatively binds to the surface, with ligand removal facilitated by time and temperature. In their study of the same precursor, Gao et al. propose that the reactions may not yet be at steady state at early cycle numbers due to lack of Ru film coalescence,[44] implying that the growth mechanism could change as a function of cycle number. While Ru species aggregation on the surface may be necessary in order for the Ru to be catalytically active,[74,75] because we find our Ru films to be smooth and coalesced at such small cycle numbers, we expect this early period of nucleation on the SiO_2 surface to be short-lived, thereby resulting in a growth mechanism that remains relatively constant during the deposition. Furthermore, in our QCM and QMS experiments we measured steady-state growth of Ru on coalesced Ru and thus we did not probe the film nucleation regime. Hence, we focus here on a model of steady state growth.

A schematic of our proposed growth mechanism for a Ru-covered surface is shown in Figure 6. In the first step of the proposed mechanism, $Ru(DMBD)(CO)_3$ binds dissociatively to the surface, where surface Ru sites active to $Ru(DMBD)(CO)_3$ reaction are denoted by Ru*, preferentially releasing the DMBD ligand as modeled by Gao et al.[44] and Kim et al.[76] and potentially also releasing some fraction of the CO ligands. The release of DMBD in this step is consistent with the QMS results which show evolution of DMBD, as illustrated in Figure 3.

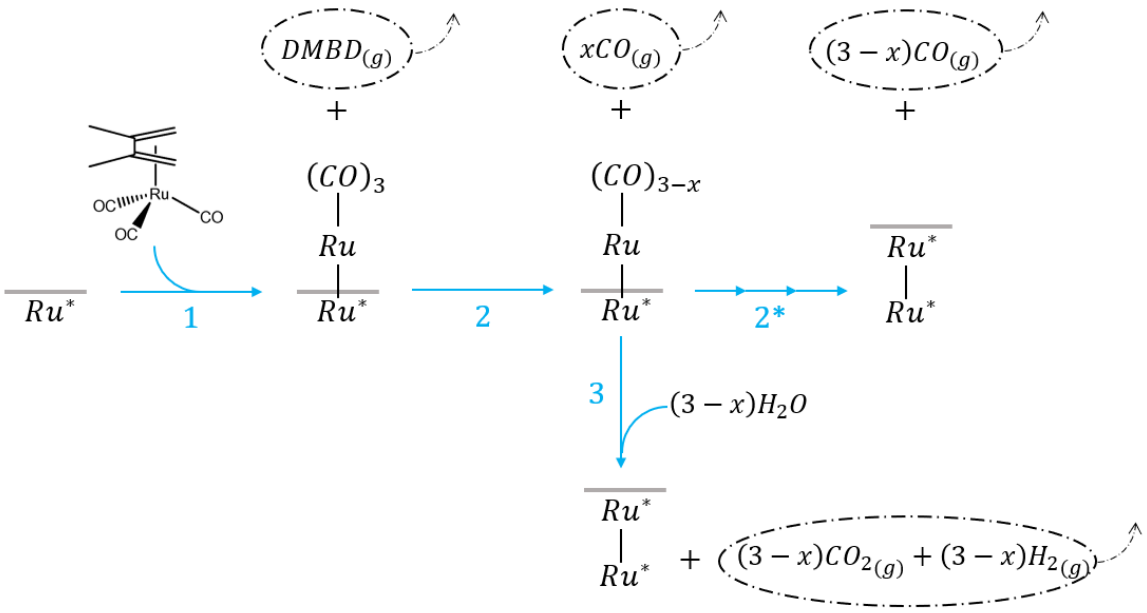

Figure 6. Schematic of the proposed mechanism of $Ru(DMBD)(CO)_3$ reaction with the surface under steady state deposition conditions. In step (1) Ru precursor dissociatively chemisorbs to the Ru surface preferentially releasing DMBD, followed by (2) spontaneously releasing some CO ligands from the surface, and (2*) further CO release to completion resulting in a pristine Ru surface. Step (3) depicts a WGS reaction with H_2O that could take place if step (2) does not progress to completion, but we do not observe conclusive evidence of this step occurring.

Once the Ru species have adsorbed to the surface, they can continue to lose CO ligands according to step 2. Because this is a thermally activated reaction, the extent of loss of the surface-passivating CO ligands is determined by reaction conditions, with increasing temperature and time resulting in increasing extent of reaction as indicated by step 2*. We propose that with sufficient CO ligands remaining on the Ru metal center, the adsorbed complex is unreactive toward additional $Ru(CMBD)(CO)_3$ precursor molecules and adsorption is saturated (self-limiting regime). On the other hand, once most or all CO ligands have been released, the Ru metal center becomes a new active surface site and deposition is no longer self-limiting during precursor exposure. The QCM data in Figure 2 indicate that we access both of these regimes

experimentally, depending on conditions. Namely, at temperatures at or below 100 °C and at reaction timescales at or below 5 seconds (the single pulse timescale), the CO ligand release rate is slow enough for the reaction to be self-limiting, with enough passivating CO ligands remaining on the surface (step 2 is incomplete). However, at higher temperatures and longer timescales, the CO ligand loss occurs rapidly enough to create sufficient new surface active sites (step 2 is complete through 2*) that allow for further non-limiting precursor reaction (step 1).

Under conditions in which the CO ligand release does not proceed to full completion (akin to step 2 not proceeding fully through 2*), e.g., at short timescales and low temperatures, the work by Gao et al. suggests that H_2O in the subsequent pulse might participate in the WGS reaction (step 3).[44,77] However, we find no confirmation that the WGS reaction is occurring, particularly in CO_2 measurements by QMS which do not show strong evidence for CO_2 generation. The absence of detectable CO_2 product of the WGS reaction in the QMS measurements may potentially be explained by Ru activity as described below or by the fast loss of all CO ligands (per pathway 2*) on the timescale of H_2O introduction under most of the conditions studied in this work (deposition temperatures from 100 to 180 °C), consistent with existing work on CO desorption from Ru surfaces at these temperatures.[78] Use of shorter timescales would prove difficult, as seen by the incomplete purging in Figure S2a-b and Figure S5. On the other hand, at the lowest deposition temperature of 80 °C, our results show that CO ligands are retained in the film. A GPC of less than 0.1 Å/cycle in Figure 5a and Figure S1 indicates passivating CO ligands persist to inhibit growth under these conditions, which combined with the observation of impurities demonstrates that H_2O does not play a significant role in removing CO ligands. This lack of reactivity is not surprising given the body of heterogeneous catalysis work showing Ru has low activity towards the WGS reaction across a

range of supports and conditions at such low temperatures.[62–66] More reactive counter-reactants like O_2 or other methods of introducing energy such as electron exposure could be more effective than water at ligand elimination under these conditions.[34]

In general, as seen in Figure 4, Figure 5, and Figures S6-8, at all deposition temperatures and reaction timescales, the addition of H_2O plays no significant role on the Ru deposition process. We observe by XPS that the presence of water has no effect on impurity levels in the film. The results of XRR and XRD also show no consistent difference in density or quality of the film correlated with the presence of water in the process, and finally, we find no evidence of increased growth rate with the presence of water (Figure S2). Importantly, there is a direct route possible, in which H_2O is not necessary, for elimination of the CO ligands from the precursor. Depending on the structure of the Ru complex and presence of other species, the Ru-CO bond energy is only approximately 10-40 kcal/mol,[44,79–81] meaning CO is relatively labile at the temperatures under study. Moreover, CO desorption does not change the oxidation state of the Ru center, and there is an entropic driving force for the release of gaseous CO from the surface, hence we would expect this process to be facile and rapid at elevated temperatures. As we will confirm with kinetic modeling, our data are consistent with this bond energy and with a spontaneous CO desorption reaction, and at the relevant timescales our model predicts a desorption rate rapid enough that H_2O participation in the reaction is negligible.

The proposed growth mechanism is also consistent with other literature reports of zero-oxidation state precursors. The observation that growth rate increases with temperature suggests precursor chemisorption and ligand release play a key role in the mechanism, with higher temperatures driving ligand release further to completion, resulting in increased rates of precursor chemisorption. This pathway would also result in a non-saturating dependence of

growth on precursor exposure, consistent both with our observations and those of several recent publications. In work on a similar Ru carbonyl derivative, $Ru(C_6H_8)(CO)_3$, by Lee et al.,[80] the authors found that precursor adsorption was not self-limiting given sufficiently long purge times and exposures, suggesting that ligand desorption strongly influences growth. A recent investigation of another Ru carbonyl precursor, $Ru_2[\mu_2\text{-}\eta^3\text{-}N(t\text{Bu})\text{-}C(H)\text{-}C(i\text{Pr})](CO)_6$ (T-Rudic), also found growth behaviors in agreement with our proposed mechanism.[76] The authors observed increasing growth with temperature, including GPCs well above a monolayer per cycle at the highest temperatures studied, consistent with the thermally driven release of the precursor's L-type ligands. The authors also tested the precursor with O_2 and H_2O as counter-reactants as well as with no counter-reactant and found similar growth behaviors regardless of the choice, except for at the lowest end of the temperature range.[76] At low temperatures, they also found that ligands were incorporated into the film, requiring annealing to remove, further consistent with our observations and proposed mechanism of increased ligand persistence at lower temperatures. Another study by Liao and Ekerdt of both $Ru_3(CO)_{12}$ and ruthenium bis(di-t-butylacetamidinate) dicarbonyl $[Ru(^t\text{Bu-Me-amd})_2(CO)_2]$ precursors observed that growth rate increased with temperature, without evidence of CO decomposition into other inert species such as graphitic carbon, again in line with our proposed mechanism involving simple CO desorption.[82]

Further evidence for this mechanism of growth dependence on CO release is found in a recent ALD report of $Mo(CO)_6$ use to synthesize MoS_2 with H_2S.[39] While that system contains a different metal center and reacts on a different growth surface, $Mo(CO)_6$ is a zero-oxidation state precursor containing CO ligands, similar to $Ru(DMBD)(CO)_3$. Zeng et al. found that at lower temperatures and purge times, the CO ligands were not completely removed and were

instead incorporated into the film as impurities. They observed a high sensitivity of the film growth on dissociation of CO ligands in the precursor exposure step rather than by H_2S in the counter-reactant exposure step, closely paralleling our findings that the process and final film properties are not sensitive to the H_2O exposure step. To achieve ALD growth, Zeng et al. found that the process needed to operate in a narrow regime where CO ligand desorption was sufficiently favorable to eliminate them from the surface but not so favorable as to render precursor chemisorption non-self-limiting. The similarity of observed behaviors to the present work provides further support to our proposed mechanism.

The proposed mechanism also explains the discrepancies between previous reports of $Ru(DMBD)(CO)_3$. Because the current work reveals non-limiting precursor deposition at nearly all of the temperatures studied in those literature reports,[34,43,44] we would expect the growth rates to be highly dependent on both temperature and precursor exposure. This sensitivity, combined with the facile decomposition of the precursor on the reactor walls, could amplify differences or errors in temperature monitoring and precursor dosing across different deposition systems.

E. Kinetic Modeling

To further investigate whether the proposed mechanism is consistent with our experimental observations, we performed kinetic modeling. Because we expect the dominant mechanism to be dissociative adsorption of $Ru(DMBD)(CO)_3$ at the surface followed by CO ligand release with little participation from H_2O, we modeled only steps 1 and 2/2*. The model is not intended for rigorous quantitative analysis but rather to assess qualitative alignment of our experimental observations with the proposed mechanism; hence a few simplifications are made

in its construction. The model is used to assess if the growth trends have any physical basis in the kinetically limited phenomenon of spontaneous CO ligand desorption, and if the energetics of such a mechanism are reasonable. A derivation of the model is included in the Supplemental Information, and a more detailed discussion of the limitations and the interpretations of the modeling will follow the results below.

The kinetic model predicts the non-limiting mass gain, denoted NLMG, per Ru precursor exposure as measured by QCM in the regimes where growth continues linearly with precursor exposure without saturation (details of this calculation are provided in the Methods). The kinetic model is given by the following equation:

$$\frac{NLMG}{\Phi_{Ru}} = B \cdot \left(1 - \exp\left(-A \cdot \exp\left(-\frac{E_a}{R \cdot T}\right) \cdot t_{total}\right)\right)$$

The equation contains three known quantities from the experimental data: deposition temperature T, total reaction timescale t_{total}, and non-limiting mass gain per exposure $\frac{NLMG}{\Phi_{Ru}}$ where Φ_{Ru} represents exposure. Other variables are B, an arbitrary proportionality constant, A, the CO desorption Arrhenius exponential prefactor, E_a, the activation energy barrier for CO ligand desorption, and R, the ideal gas constant. Temperature is directly controlled in the reactor conditions, and as previously discussed, the total timescales probed in QCM depositions spanned three ranges: single pulse (~3 s), micropulse (~12 s), and multiple pulse (~44 s). As described in the Methods, NLMG per exposure can be extracted from the slopes of the linear regimes of the QCM data where non-limiting growth is observed with increasing $Ru(DMBD)(CO)_3$ exposure. For each pair of temperatures and timescales, a non-limiting growth per exposure can be extracted from the QCM measurements. The multidimensional model can then be fit to the set of data, using three fit parameters: B, A and E_a.

The result of fitting the kinetic model to the QCM data is shown in Figure 7. Figure 7a contains a contour plot depicting the experimental and modeled QCM non-limiting mass gain per exposure across a range of both timescale and temperature, and Figure 7b illustrates only one-dimensional slices of the fitted model overlaid with the experimental data with propagated error bars (as detailed in the Methods). The dashed curves in Figure 7b indicate the predicted non-limiting growth at 3 s, 12 s, and 44 s reaction timescales, approximately corresponding to the three purge timescales probed by QCM. In both plots it is apparent the model fits well—both visually to the overall trend of the data and quantitatively with an R^2 value of 0.997—despite the simplifications made in its derivation. The result yields fit parameter values of $B = 1966$, $A = 6.2 \times 10^{10}\ \mathrm{s}^{-1}$, and $E_a = 24.7\ \mathrm{kcal/mol}$. A confidence interval constructed using a parametric bootstrap algorithm propagating the error shown in Figure 7b results in a 95% confidence interval for E_a of (24.66. 27.74). The value of A is the right order of magnitude for typical Arrhenius prefactors, and an activation energy barrier of 24.7 kcal/mol is firmly within the 10-40 kcal/mol of reported Ru-CO bond strengths.[44,78–81] Furthermore, the confidence interval for E_a still lies well within this range, indicating our findings are sound amidst propagation of experimental and regression error.

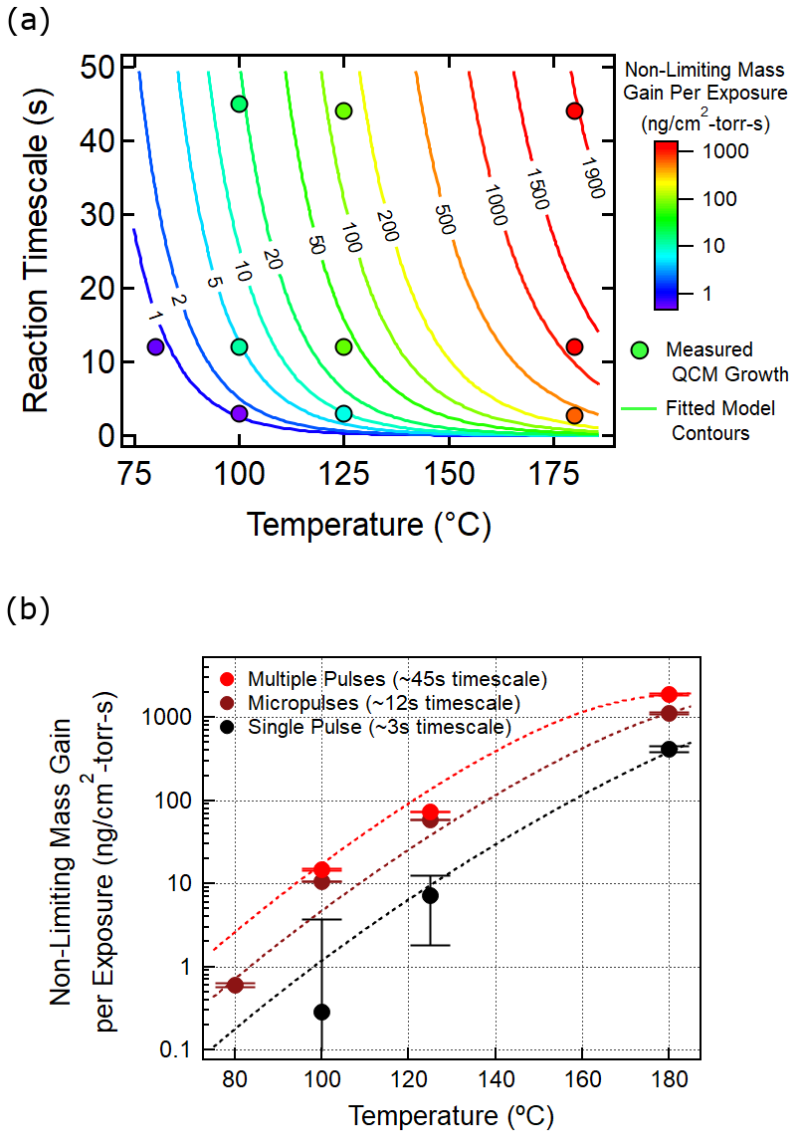

Figure 7. Kinetic modeling results of non-limiting Ru film growth from $Ru(DMBD)(CO)_3$ based on a mechanism of spontaneous CO desorption. (a) A 2D contour plot of experimental QCM data and the kinetic model fitted to that data. (b) 1D slices of the 2D model at 3 different reaction timescales (black, dark red, and light red), overlaid with experimental QCM non-limiting growths and associated propagated errors.

While assumptions were made in the construction of this simple model, it predicts the overall experimentally observed behavior of the system quite well, and it results in physically

relevant parameters consistent with prior work. Furthermore, as can be seen from the increased spacing between the contours in the upper right corner of Figure 7a, the modeled NLMG per exposure saturates with both increased reaction timescale and temperature. This outcome is physically consistent with the behavior of the system, since with sufficiently long purge time or high enough temperature, all the passivating CO ligands will desorb from the surface, in accordance with step 2* occurring to completion in Figure 6. Complete ligand desorption would result in fully non-limiting growth in which growth is only determined by exposure of the Ru precursor to the surface, i.e., growth per exposure approaches a constant. This behavior is reflected both in the mathematical form of the model, which approaches a constant value with increasing t_{total} and temperature, and in the contour plot in Figure 7a.

However, there are also limits to how closely the model aligns with physical phenomena. The model assumes all CO ligands on a given surface site desorb in a single step with a single activation barrier in a first order reaction. This assumption has been made elsewhere in studying CO desorption kinetics on flat Ru(001) surfaces[78] but could be overly simplistic and is not consistent with previous work for $Ru_3(CO)_{12}$.[54] This model also does not account for effects of neighboring sites such as potential steric effects of CO ligands blocking access to neighboring sites, which we might expect given the large size of the $Ru(DMBD)(CO)_3$ precursor. To avoid overfitting the data and for the purposes of a simple estimate of a Ru-CO bond strength, however, this simplified mean field approach is sufficient. It is apparent in Figure 7b that the multiple pulse timescale model consistently overpredicts mass gain and that the micropulse curve consistently underpredicts mass gain, and a more complete kinetic treatment considering site interactions, multiple steps, or non-first order reactions might address these discrepancies at different timescales. In addition, the model assumes that because the activation barrier for

precursor chemisorption is lower than for CO ligand removal, its rate is much more rapid and relatively constant with temperature. This assumption may be less accurate at lower temperatures where the rate could be more limited by precursor chemisorption than predicted.

F. Application & Process Design

As demonstrated in the mechanism proposed and modeled in this work, this zero-oxidation state, carbonyl-based precursor structure means it is very sensitive to process parameters such as temperature, purge time, and pulse time, and these must be carefully considered in process design. In addition, the kinetic model illustrates the role of the M-CO bond strength: if it is too low relative to the thermal energy provided then the ease of ligand dissociation will result in non-limited precursor deposition, and if it is too high then ligands will persist on the surface and either introduce impurities into the film or require stronger conditions to remove. The sensitivity of growth to these parameters and the inconsistency in literature reports of $Ru(DMBD)(CO)_3$ stress the importance of rigorous saturation characterization for similar precursors. If ligand desorption from the surface is sufficiently facile to occur spontaneously on the timescale of the purge time but more slowly than the exposure time, it is possible for saturation studies to provide an incomplete or misleading picture. Since ALD saturation curves are often generated by increasing the precursor pulse time, if this is not enough time for the passivating ligands to desorb then self-limiting growth will be observed, as is typically desired. However, the process may not be truly self-limiting but rather appear so only because of insufficient time provided for the precursor to react, thereby leading to misleading understandings of the role of the counter-reactant and the chemical state of the surface.

Instead, to fully establish the conditions under which self-limiting growth holds and the timescale for which passivating ligands remain on the surface, it is helpful to perform experiments where either (i) precursor exposure is increased not by increasing pulse time but by adding repeated pulses, such as in Figure 1 and Figure 2a, or (ii) where the precursor alone is dosed repeatedly with no counter-reactant. Extremely long pulses on the scale of total needed reaction time are a possible alternative to (i), though this could be impractical and prone to misleading conclusions as described above.

Finally, we note that the type of non-self-limiting behavior seen in zero-oxidation state precursors that grow by a mechanism similar to $Ru(DMBD)(CO)_3$ may be desirable in certain applications. Growth via a CVD-like mechanism can be helpful in systems that do not face uniformity or conformality challenges but that benefit from increased growth rates or improved film properties or require high-purity films.[83] Moreover, when depositing on 3-dimensional substrates for which mass transport considerations become significant, non-limiting growth can still be used to achieve conformal and superconformal films in deep features,[84–86] but it is important to consider the process design considerations that differ between CVD and ALD.[1,27,87]

V. Conclusion

In this work, we demonstrate that $Ru(DMBD)(CO)_3$ is an excellent precursor for the deposition of high quality Ru films at low thicknesses and temperatures, particularly relative to temperatures typically used for metal ALD. The purity and metallic state of the films were verified by XPS, XRD, and XRR, and the films were shown by AFM and XRR to be very

smooth with little to no nucleation delay. Mechanistic studies show that the precursor releases the DMBD ligand during chemisorption to the substrate. Remaining surface CO ligands can then desorb given enough time or thermal energy. CO elimination by water through the water-gas shift reaction was not observed in this work, and no other evidence for reaction of the adsorbed precursor with the H_2O counter-reactant was found. We propose that the dominant Ru deposition mechanism is via thermal desorption of labile CO ligands, regenerating active sites for further Ru precursor adsorption. The mechanism of CO desorption was kinetically modeled and found to fit QCM data well, producing a Ru-CO bond energy consistent with previous reports. This kinetically limited desorption mechanism explains the non-limiting growth rates observed by QCM that depend on both temperature and purge times. The proposed mechanism is also consistent with other reported behaviors of related zero-oxidation state precursors and explains inconsistencies between previous studies of this precursor. Finally, this work provides insight into how saturation studies for other zero-oxidation precursors that grow by a similar mechanism ought to be designed to properly account for ligand persistence and self-limiting growth.

VI. Acknowledgements

This work was supported by the Department of Energy under Award Number DE-SC0004782. Part of this work was performed at the Stanford Nano Shared Facilities (SNSF), supported by the National Science Foundation under award ECCS-1542152.

VII. Conflict of Interest

The authors declare no conflict of interest.

VIII. References

[1] S. M. George, *Chem. Rev.* **2010**, *110*, 111.

[2] J. A. Raiford, S. T. Oyakhire, S. F. Bent, *Energy Environ. Sci.* **2020**, *13*, 1997.

[3] A. S. Asundi, J. A. Raiford, S. F. Bent, *ACS Energy Lett.* **2019**, *4*, 908.

[4] J. Plutnar, M. Pumera, *Small* **2021**, 2102088.

[5] J. E. Mondloch, W. Bury, D. Fairen-Jimenez, S. Kwon, E. J. Demarco, M. H. Weston, A. A. Sarjeant, S. T. Nguyen, P. C. Stair, R. Q. Snurr, O. K. Farha, J. T. Hupp, *J. Am. Chem. Soc.* **2013**, *135*, 10294.

[6] A. W. Peters, Z. Li, O. K. Farha, J. T. Hupp, *ACS Nano* **2015**, *9*, 8484.

[7] A. J. M. Mackus, J. R. Schneider, C. Macisaac, J. G. Baker, S. F. Bent, *Chem. Mater.* **2019**, *31*, 1142.

[8] J. R. Abelson, G. S. Girolami, *J. Vac. Sci. Technol. A* **2020**, *38*, 030802.

[9] V. Cremers, R. L. Puurunen, J. Dendooven, *Appl. Phys. Rev.* **2019**, *6*, 21302.

[10] S. D. Elliott, G. Dey, Y. Maimaiti, H. Ablat, E. A. Filatova, G. N. Fomengia, *Adv. Mater.* **2016**, *28*, 5367.

[11] C. De Paula, N. E. Richey, L. Zeng, S. F. Bent, *Chem. Mater.* **2020**, *32*, 315.

[12] R. L. Puurunen, *J. Appl. Phys.* **2005**, *97*, DOI 10.1063/1.1940727.

[13] J. R. Schneider, J. G. Baker, S. F. Bent, *Adv. Mater. Interfaces* **2020**, *7*, 2000318.

[14] J. G. Baker, J. R. Schneider, J. A. Raiford, C. de Paula, S. F. Bent, *Chem. Mater.* **2020**, *32*,

1925.

[15] S. D. Elliott, O. Nilsen, *ECS Trans.* **2011**, *41*, 175.

[16] E. Thimsen, Q. Peng, A. B. F. Martinson, M. J. Pellin, J. W. Elam, *Chem. Mater.* **2011**, *23*, 4411.

[17] A. J. M. Mackus, C. MacIsaac, W.-H. Kim, S. F. Bent, *J. Chem. Phys.* **2017**, *146*, 052802.

[18] V. Vandalon, W. M. M. Kessels, *Appl. Phys. Lett.* **2016**, *108*, 011607.

[19] J. W. Elam, S. M. George, *Chem. Mater.* **2003**, *15*, 1020.

[20] V. Miikkulainen, M. Leskelä, M. Ritala, R. L. Puurunen, *J. Appl. Phys.* **2013**, *113*, 21301.

[21] B. Hudec, K. Hušeková, A. Tarre, J. H. Han, S. Han, A. Rosová, W. Lee, A. Kasikov, S. J. Song, J. Aarik, C. S. Hwang, K. Fröhlich, *Microelectron. Eng.* **2011**, *88*, 1514.

[22] K. Kukli, M. Ritala, T. Sajavaara, J. Keinonen, M. Leskelä, *Thin Solid Films* **2002**, *416*, 72.

[23] W.-J. Lee, J.-H. Lee, Y.-S. Lee, S.-K. Rha, C.-O. Park, *Korean J. Mater. Res.* **2004**, *14*, 141.

[24] S. Kamiyama, T. Miura, Y. Nara, *Thin Solid Films* **2006**, *515*, 1517.

[25] M. B. E. Griffiths, Z. S. Dubrawski, G. Bačić, A. Japahuge, J. D. Masuda, T. Zeng, S. T. Barry, *Eur. J. Inorg. Chem.* **2019**, *2019*, 4927.

[26] W. J. Lee, Z. Wan, C. M. Kim, I. K. Oh, R. Harada, K. Suzuki, E. A. Choi, S. H. Kwon, *Chem. Mater.* **2019**, *31*, 5056.

[27] R. W. Johnson, A. Hultqvist, S. F. Bent, *Mater. Today* **2014**, *17*, 236.

[28] S. Xu, Y. Kim, J. Park, D. Higgins, S. J. Shen, P. Schindler, D. Thian, J. Provine, J. Torgersen, T. Graf, T. D. Schladt, M. Orazov, B. H. Liu, T. F. Jaramillo, F. B. Prinz, *Nat. Catal.* **2018**, *1*, 624.

[29] M. W. Lane, C. E. Murray, F. R. McFeely, P. M. Vereecken, R. Rosenberg, *Appl. Phys. Lett.* **2003**, *83*, 2330.

[30] K. Frohlich, B. Hudec, M. Tapajna, K. Husekova, A. Rosova, P. Elias, J. Aarik, R. Rammula, A. Kasikov, T. Arroval, L. Aarik, K. Murakami, M. Rommel, A. J. Bauer, *ECS Trans.* **2013**, *50*, 79.

[31] J. Hämäläinen, M. Ritala, M. Leskelä, *Chem. Mater.* **2014**, *26*, 786.

[32] S. Dutta, S. Kundu, A. Gupta, G. Jamieson, J. F. G. Granados, J. Bömmels, C. J. Wilson, Z. Tokei, C. Adelmann, *IEEE Electron Device Lett.* **2017**, *38*, 949.

[33] L. G. Wen, P. Roussel, O. V. Pedreira, B. Briggs, B. Groven, S. Dutta, M. I. Popovici, N. Heylen, I. Ciofi, K. Vanstreels, F. W. Østerberg, O. Hansen, D. H. Petersen, K. Opsomer, C. Detavernie, C. J. Wilson, S. Van Elshocht, K. Croes, J. Bömmels, Z. Tökei, C. Adelmann, *ACS Appl. Mater. Interfaces* **2016**, *8*, 26119.

[34] D. Z. Austin, M. A. Jenkins, D. Allman, S. Hose, D. Price, C. L. Dezelah, J. F. Conley, *Chem. Mater.* **2017**, *29*, 1107.

[35] M. Diskus, O. Nilsen, H. Fjellvåg, *J. Mater. Chem.* **2011**, *21*, 705.

[36] Z. Jin, S. Shin, D. H. Kwon, S.-J. Han, Y.-S. Min, *Nanoscale* **2014**, *6*, 14453.

[37] F. Zaera, *Surf. Sci.* **1991**, *255*, 280.

[38] M. Xu, F. Zaera, *J. Vac. Sci. Technol. A Vacuum, Surfaces, Film.* **1996**, *14*, 415.

[39] L. Zeng, N. E. Richey, D. W. Palm, I.-K. Oh, J. Shi, C. Maclsaac, T. Jaramillo, S. F. Bent, *J. Vac. Sci. Technol. A* **2020**, *38*, 060403.

[40] Z. Song, T. Cai, J. A. Rodriguez, J. Hrbek, A. S. Y. Chan, C. M. Friend, *J. Phys. Chem. B* **2003**, *107*, 1036.

[41] R. Gaur, L. Mishra, M. A. Siddiqi, B. Atakan, *RSC Adv.* **2014**, *4*, 33785.

[42] M. E. Gross, *J. Vac. Sci. Technol. B Microelectron. Nanom. Struct.* **1988**, *6*, 1548.

[43] S. Cwik, K. N. Woods, M. J. Saly, T. J. Knisley, C. H. Winter, *J. Vac. Sci. Technol. A* **2020**, *38*, 012402.

[44] Z. Gao, D. Le, A. Khaniya, C. L. Dezelah, J. Woodruff, R. K. Kanjolia, W. E. Kaden, T. S. Rahman, P. Banerjee, *Chem. Mater.* **2019**, *31*, 1304.

[45] M. Hayes, M. A. Jenkins, J. Woodruff, D. F. Moser, C. L. Dezelah, J. F. ConleyJr., *J. Vac. Sci. Technol. A Vacuum, Surfaces, Film.* **2021**, *39*, 052402.

[46] T. E. Hong, S.-H. Choi, S. Yeo, J.-Y. Park, S.-H. Kim, T. Cheon, H. Kim, M.-K. Kim, H. Kim, *ECS J. Solid State Sci. Technol.* **2013**, *2*, P47.

[47] S.-H. Choi, T. Cheon, S.-H. Kim, D.-H. Kang, G.-S. Park, S. Kim, *J. Electrochem. Soc.* **2011**, *158*, D351.

[48] W.-J. Lee, S. Bera, H.-J. Woo, J.-W. An, J.-S. Bae, I.-K. Oh, S.-H. Kwon, *J. Mater. Chem. A* **2021**, *9*, 17223.

[49] G. Liu, J. Woodruff, D. F. Moser, M. Moinpour, R. K. Kanjolia, in *Int. Interconnect Technol. Conf. - 2019 IITC MAM Progr.*, **2020**.

[50] C. H. Winter, in *Am. Vac. Soc. 20th Int. Conf. At. Layer Depos.*, **2020**.

[51] F. Zaera, *Tungsten Hexacarbonyl Thermal Decomposition on Ni(100) Surfaces*, **1992**.

[52] C. C. Cho, S. L. Bernasek, *J. Appl. Phys.* **1989**, *65*, 3035.

[53] A. Theolier, A. Choplin, L. D'Ornelas, J. M. Basset, G. Zanderighi, C. Sourisseau, *Polyhedron* **1983**, *2*, 119.

[54] G. M. Zanderighi, C. Dossi, R. Ugo, R. Psaro, A. Theolier, A. Choplin, L. D'Ornelas, J. M. Basset, *J. Organomet. Chem.* **1985**, *296*, 127.

[55] P. Zhang, E. Mohimi, T. K. Talukdar, J. R. Abelson, G. S. Girolami, *J. Vac. Sci. Technol. A Vacuum, Surfaces, Film.* **2016**, *34*, 051518.

[56] P. Mohanty, K. K. Pant, S. N. Naik, J. Parikh, A. Hornung, J. N. Sahu, *Renew. Sustain. Energy Rev.* **2014**, *38*, 131.

[57] V. Y. Vasilyev, K. P. Mogilnikov, Y. W. Song, *J. Electrochem. Soc.* **2008**, *155*, D763.

[58] J. Ilavsky, *J. Appl. Crystallogr.* **2012**, *45*, 324.

[59] J. H. Hubbell, S. M. Seltzer, *X-Ray Mass Attenuation Coefficients, NIST Standard Reference Database 126*, National Institute Of Standards And Technology, Gaithersburg MD, **2004**.

[60] J. A. Dean, *Lange's Handbook of Chemistry*, McGraw-Hill, **1999**.

[61] R. Lucklum, F. Eichelbaum, in *Piezoelectric Sensors*, Springer Berlin Heidelberg, **2006**, pp. 3–47.

[62] A. Venugopal, M. S. Scurrell, *Appl. Catal. A Gen.* **2003**, *245*, 137.

[63] A. Venugopal, J. Aluha, D. Mogano, M. S. Scurrell, *Appl. Catal. A Gen.* **2003**, *245*, 149.

[64] N. Liu, L. Guo, Z. Cao, W. Li, X. Zheng, Y. Shi, J. Guo, Y. Xi, *J. Phys. Chem. A* **2016**, *120*, 2408.

[65] J. J. Verdonck, P. A. Jacobs, J. B. Uytterhoeven, *J. Chem. Soc. Chem. Commun.* **1979**, 181.

[66] G. A. de Queiroz, C. M. B. de Menezes Barbosa, C. A. M. de Abreu, *React. Kinet. Mech. Catal. 2018 1232* **2018**, *123*, 573.

[67] P. C. Ford, *Acc. Chem. Res.* **1981**, *14*, 31.

[68] R. M. Laine, R. G. Rinker, P. C. Ford, *J. Am. Chem. Soc.* **1977**, *99*, 252.

[69] J. C. Bricker, C. C. Nagel, S. G. Shore, *J. Am. Chem. Soc.* **1982**, *104*, 1444.

[70] N. E. Richey, C. De Paula, S. F. Bent, *J. Chem. Phys.* **2020**, *152*, 40902.

[71] G. Wypych, *Handbook of Polymers*, Elsevier, Ontario, Canada, **2012**.

[72] J. Als-Nielsen, D. McMorrow, *Elements of Modern X-Ray Physics*, John Wiley & Sons, Inc., Hoboken, NJ, USA, **2011**.

[73] A. Nelson, *J. Appl. Crystallogr.* **2006**, *39*, 273.

[74] S. H. Joo, J. Y. Park, J. R. Renzas, D. R. Butcher, W. Huang, G. A. Somorjai, *Nano Lett.* **2010**, *10*, 2709.

[75] J. Soethoudt, F. Grillo, E. A. Marques, J. R. van Ommen, Y. Tomczak, L. Nyns, S. Van Elshocht, A. Delabie, *Adv. Mater. Interfaces* **2018**, *5*, 1800870.

[76] H.-M. Kim, J.-H. Lee, S.-H. Lee, R. Harada, T. Shigetomi, S. Lee, T. Tsugawa, B. Shong,

J.-S. Park, *Chem. Mater.* **2021**, DOI 10.1021/acs.chemmater.0c04496.

[77] D. S. Newsome, *Catal. Rev.* **1980**, *21*, 275.

[78] H. Pfnür, P. Feulner, D. Menzel, *J. Chem. Phys.* **1983**, *79*, 4613.

[79] A. W. Ehlers, G. Frenking, *Organometallics* **1995**, *14*, 423.

[80] J. Lee, Y. W. Song, K. Lee, Y. Lee, H. K. Jang, *ECS Trans.* **2019**, *2*, 1.

[81] P. L. Bogdan, E. Weitz, *J. Am. Chem. Soc.* **1989**, *111*, 3163.

[82] W. Liao, J. G. Ekerdt, *J. Vac. Sci. Technol. A Vacuum, Surfaces, Film.* **2016**, *34*, 041514.

[83] M. E. Dufond, M. W. Diouf, C. Badie, C. Laffon, P. Parent, D. Ferry, D. Grosso, J. C. S. Kools, S. D. Elliott, L. Santinacci, *Chem. Mater.* **2020**, *32*, 1393.

[84] W. B. Wang, N. N. Chang, T. A. Codding, G. S. Girolami, J. R. Abelson, *J. Vac. Sci. Technol. A Vacuum, Surfaces, Film.* **2014**, *32*, 051512.

[85] A. Yanguas-Gil, Y. Yang, N. Kumar, J. R. Abelson, *J. Vac. Sci. Technol. A Vacuum, Surfaces, Film.* **2009**, *27*, 1235.

[86] A. Yanguas-Gil, N. Kumar, Y. Yang, J. R. Abelson, *J. Vac. Sci. Technol. A Vacuum, Surfaces, Film.* **2009**, *27*, 1244.

[87] A. Sherman, *Chemical Vapor Deposition for Microelectronics: Principles, Technology and Applications*, Noyes Publications, Park Ridge, NJ, **1987**.